



Corrosion Properties of Heterostructured [8YSZ/Al₂O₃]_n Coatings as a Function of the Bilayer Number

C.H. Ortiz , J.C. Caicedo, and W. Aperador

Submitted: 5 May 2021 / Revised: 23 August 2021 / Accepted: 19 September 2021 / Published online: 18 October 2021

This study presents a detailed analysis of the wear presented in [8YSZ/ α -Al₂O₃] multilayer coatings as a function of the bilayer number when exposed to a corro-erosive environment. In this study, the roughness and grain size decreased by 58 and 30%, respectively when comparing the 70 bilayers system with the 1 bilayer system. The surface factors and the higher bilayer number of the $n = 70$ system, influenced the 67.33% decrease in corrosion rate compared to the 1 bilayer system. Subsequently, by means of SEM and optical microscopy, the degradation of the coatings due to the impact of abrasive particles and the generation of oxides on the substrate surface caused by a partial delamination of the coating was evidenced. This wear was calculated by means of the mass loss after the corro-erosive test, obtaining a decrease of 55.25% for the system with 70 bilayers with respect to the system with 1 bilayer. The results obtained showed that the system with 70 bilayers presented the best set of electrochemical properties and lower wear in corrosive environments, which makes it the best candidate to be used as a protective coating.

Keywords abrasive particles, corrosive–erosive study, corrosive degradation, electrochemical properties, thermal barrier coating

1. Introduction

Conventional thermal barrier coatings (TBCs) are multilayer systems used with the main purpose of providing thermal protection to devices implemented in applications such as turbines, motors, engines, among others. The focus of these coatings is based on reducing the impact of the thermal and corrosive shock on the components coated with this type of coating (Ref 1, 2). In addition, an important part of these coatings is their resistance to highly oxidizing and highly aggressive environments, which is attributed to the fact that conventional TBC systems are composed of three layers; a metal bonding layer (BC), an intermediate oxide layer (TGO), and a ceramic top layer (TC), where the surface layer (TC) is the main one in providing important characteristics such as oxidation resistance and thermal expansion. These are all main factors that are related to the service life of TBCs (Ref 3, 4).

All these layers have different physical, mechanical, thermal, and electrochemical properties, which are strongly affected by their processing conditions. Over the years, TBCs have evolved from layers for insulating applications only, to more complex designs that are implemented in applications where high mechanical, tribological and great corrosion resistance properties are required. Currently, these types of systems have been deposited or synthesized in a wide variety of commercial

techniques, including air plasma sputtering (APS) (Ref 5), electron beam physical vapor deposition (EB-PVD) (Ref 6), physical vapor deposition (PVD) (Ref 2), and the sol-gel process (Ref 7), among others. The physical vapor deposition (PVD) process by magnetron sputtering produces TBCs with thicknesses between 1 and 3 μm . Although these coatings are much thinner than those obtained by traditional techniques (APS and EB-PVD), the PVD technique allows depositing TBC which shows excellent corrosion resistance while maintaining good thermal insulation properties. This behavior is attributed to the grain size obtained through this particular synthesis process, which is in the nanometric range. Since phonon dispersion increases because surface-volume fraction improves, an additional mechanism is provided that significantly reduces the thermal conductivity by decreasing the grain size. Moreover, by the nucleation effect in the multilayer systems, the growth of the grains is interrupted by the deposition of a new layer; therefore, multilayer systems are obtained with nano-sized grains that will directly influence the electrochemical properties of the coatings (Ref 8, 9).

A recent investigation of the TBC system has shown that [YSZ/Al₂O₃]_n coatings have demonstrated good thermal cycling and thermal degradation performance due to the properties of their individual layers. The YSZ ceramic layer has been widely used due to its low thermal conductivity, high phase stability, high thermal expansion coefficient, and high fracture toughness, among other characteristics (Ref 10). The Al₂O₃-based coating exhibits important characteristics such as good mechanical properties, wear resistance and crack resistance, as well as good adhesion to the substrate (Ref 11). This set of properties has made the [8YSZ/Al₂O₃]_n multilayer system an ideal candidate to be chosen as a protective coating for high temperature applications. Currently, the [8YSZ/Al₂O₃] multilayer system has studies focused on its resistance to thermal cycling (Ref 2), electrochemical studies at various temperatures (Ref 12), mechanical studies (Ref 13), among others. However, this system does not have electrochemical studies that can emphatically and concisely express the behavior of this multilayer system in a corrosive–erosive

C.H. Ortiz and J.C. Caicedo, Tribology, Polymers, Powder Metallurgy and Solid Waste Transformations Research Group, Universidad del Valle, Cali, Colombia; and W. Aperador, Engineering School, Universidad Militar Nueva Granada, Bogotá, Colombia. Contact e-mail: christian.ortiz.ortiz@correounivalle.edu.co.

environment. For this reason, the main purpose of this research was to perform a detailed and systematic study of the effects of the $[8YSZ/Al_2O_3]_n$ multilayer coatings electrochemical properties on the surface wear generated in corrosive-erosive environments. This was done in order to predict their performance in applications as protective coatings in highly aggressive environments.

2. Experimental Procedure

2.1 Materials

The AISI 304 steel substrates were obtained from the BÖHLER Company in a state of supply with a cylindrical shape, having a 1/2 in. diameter of and a thickness of 5 mm. The percentage by weight of the elements is presented in Table 1. These substrates were duly prepared superficially by means of (SiC) sandpaper, following the order of 80, 100, 120, 240, 320, 400, 600, 800, 1000, and 1200 μm . After that, they were polished by means of a metallographic polisher using a water-alumina solution with a particle size between 1 and 0.3 μm . Finally, a cleaning process was performed using a “Rio Grande UD50SH-2L” ultrasound for 10 min in order to remove residues from the surface. The silicon wafers used for the structural analysis were monochromatic silicon with an orientation (100) and its cleaning was also performed by ultrasound for 10 min.

The cathodes of Yttria stabilized with 8% molar zirconia (8YSZ) and alumina (Al_2O_3), with a diameter of 10 cm, had a purity of 99.99% and were obtained from the company “PLASMATERIALS”. The Argon gas had a purity of 99.99%.

2.2 Coating Synthesis

The $[8YSZ/\alpha-Al_2O_3]_n$ multilayer coatings were deposited by the multi-target magnetron reactive sputtering system using a radio frequency (r.f) source (13.56 MHz) on AISI 304 stainless steel and silicon (100) substrates in a controlled argon atmosphere (99.99%). A power of 400 W was used for both cathodes. The substrate-cathodes distance was 6 cm. The deposition of the coatings was carried out at a temperature of 250 °C and a bias voltage of -20 V. For this $[8YSZ/Al_2O_3]_n$ multilayer system, the bilayer number was systematically varied ($n = 1, 10, 30, 50, \text{ and } 70$) while maintaining a constant thickness of 1.8 μm . This corresponds to a spatial periodicity (Λ) of $\Lambda = 900 \text{ nm}$, $\Lambda = 180 \text{ nm}$, $\Lambda = 60 \text{ nm}$, $\Lambda = 36 \text{ nm}$, and $\Lambda = 26 \text{ nm}$, respectively ($\Lambda = \text{thickness}/n$).

2.3 Characterization of the Multilayer Coatings

The crystallographic structure was characterized by x-ray diffraction (XRD) with a wavelength ($\lambda = 1.5406 \text{ \AA}$) using a Bragg-Brentano configuration, high angle range. For this analysis, the appropriate equipment parameters were deter-

Table 1 Chemical composition of steel substrates

Element	C	Si	Mn	Cr	Ni	Fe
Percentage, %	0.03	0.5	1.40	18.5	9.5	70.7

mined such as the optimum incidence angle ranging from 10° to 30° and with a counting time of 1 sec for each step and at a step size of 0.003. In addition, a power of 45 kV and 40 mA was used, and to identify the phases, the ICCD database through the X’pert High Score software was used. The chemical analysis was performed using a JEOL Model JSM 6490 LV microscope in the backscattered electron mode with an acceleration voltage of 20 kV. Additionally, chemical microanalyses were carried out on several inspection areas, using the EDS probe of the Oxford Instrument Model INCA PentaFETx3. The surface characterization for all coatings was carried out with an MFP-3D equipment from Asylum Research in the no-contact mode. The measurements of roughness and grain size were obtained over an area of 5.0 $\mu\text{m} \times 5.0 \mu\text{m}$, and the results were analyzed with the scanning probe image processor program (SPIP). The electrochemical study was carried out with a Gamry unit, model PCI 4, utilized for DC and AC measurements. Electrochemical impedance spectroscopy (EIS), and Tafel polarization curves were obtained at room temperature, using a cell with a working electrode within an exposed area of 1 cm^2 , a reference electrode (Ag/AgCl) and a platinum wire counter electrode under a 3.5% NaCl solution with distilled water. For the Nyquist diagrams, a frequency sweep in the range of 100 kHz to 0.001 Hz was performed, using a sinusoidal voltage amplitude of 10 mV applied to the working electrode (sample) and reference electrode. The samples were kept in the 3.5% NaCl aqueous solution for 30 min to establish stable corrosion potential (E_{corr}) values at which the EIS measurements were initiated. Since the experimental EIS parameters, particularly the scan rate, will affect both initial and final potential after establishing a stable (E_{corr}). To obtain the Tafel polarization curve diagrams, a voltage sweep at a speed of 0.5 mV/s in the range of -0.25 to 1.0 V was used, using the ZView software. The analysis of the total mass loss by erosion damage as a function of the bilayer number was obtained by a total time of 2 h for one impact angle (90°). As for the analysis of the tribo-corrosion effects, a device built for the evaluation of chemical attack in metallic materials was used, Fig. 1. The corrosive-erosive testing device consists of a tribometer with a glass container for corrosive-erosive storage,

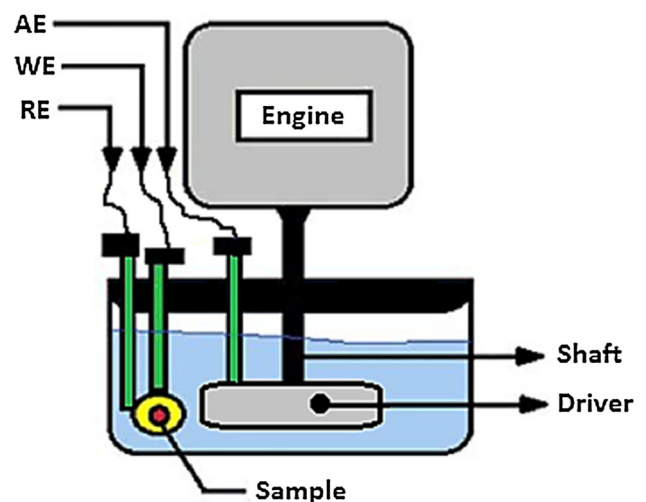


Fig. 1 Schematic of the device used in the tribo-corrosion wear test. Auxiliary electrode (AE), working electrode (WE), reference electrode (RE)

one reference and one counter electrode, as well as an acrylic cover that contains the sample holder and electrodes. Additionally, the device also has an impeller of High Ultra Molecular Weight Polyethylene which rests on a Teflon shaft that is attached to the main motor shaft. The lid of the container allowed locating two different samples exposed under angles for corrosive fluid action (90°). The corrosive fluid contained silicon particulates between 210 and $300\ \mu\text{m}$. The fluid movement was caused by the shaft driver of the motor. The speed motor was fixed to 1930 RPM, and the tangential speed applied to the fluid was fixed to 11.12 m/s.

3. Analysis and Results

3.1 Structural Analysis

Figure 2 shows the x-ray diffraction patterns of the $[\text{8YSZ}/\alpha\text{-Al}_2\text{O}_3]_n$ multilayer coatings as a function of the bilayers number $n = 1, 10, 30, 50,$ and 70 , deposited on silicon substrates. From these results, it was possible to observe the

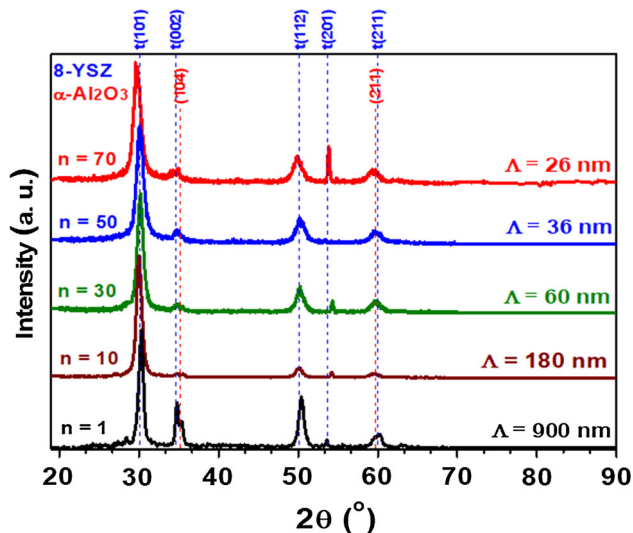


Fig. 2 Diffraction patterns for the $[\text{8YSZ}/\alpha\text{-Al}_2\text{O}_3]_n$ multilayer coatings as a function of the bilayers number (n) and periodicity (Λ)

presence of a tetragonal phase (t-8YSZ) located in the Bragg peaks $t(101)$, $t(002)$, $t(112)$, $t(201)$, and $t(211)$ for angles $2\theta = 30.29^\circ; 34.79^\circ; 50.41^\circ; 53.63^\circ;$ and 60.11° , respectively. Also observed was the presence of an alumina phase ($\alpha\text{-Al}_2\text{O}_3$), which is evident by the reflection peaks (104) and (211) at angles $2\theta = 35.32^\circ$ and 59.65° , respectively. The peaks of higher intensity corresponding to the preferential orientations of 8YSZ and $\alpha\text{-Al}_2\text{O}_3$ belong to the $t(101)$ and (104) planes, respectively. These orientations are consistent with the international denotation of indexing files JCPDS 00-048-0224 for the tetragonal structure (8YSZ) and space group $137\text{-P}42/\text{nmc}$, as well as the indexation file JCPDF 00-010-0173 indicating a rhombohedral structure for ($\alpha\text{-Al}_2\text{O}_3$) with space group $167\text{R}3\text{c}$, which have been reported in literature (Ref 12-14).

Figure 3(a) and (b) present a magnification of the peaks of highest intensity referring to each 8YSZ and $\alpha\text{-Al}_2\text{O}_3$ phase, respectively. Also shown are the positions where the materials are stress-free (dotted line). From these results, it was determined that by increasing the bilayer number (Fig. 3a) the peaks presented a shift to the left (smaller angles). This indicates the presence of compressive stresses within the crystalline structure generated by ionic bombardment during the deposition process of the coatings, these compressive stresses cause a compaction of the crystalline structure obtaining denser and more compact coatings, which influenced the surface characteristics (roughness and grain size) as corroborated in the Section 3.3. From Fig. 3(b), a decrease in preferential growth of the $\alpha\text{-Al}_2\text{O}_3$ phase and a reduction in the amplitude in the peaks as the bilayer number increased was determined. This is attributed to the effect of the non-coherent interfaces that increase as the bilayer number increment.

Figure 4 shows the percentage quantification of the phase change as a function of the bilayer number, obtained by using, Fig. 3(a) and (b), which show the magnification of the peaks of higher intensity TETRAGONAL- $t(101)$ - and ORTORHOMBICAL-(104)- belonging to the YSZ and Al_2O_3 phase, respectively. From these results, it was evidenced that there was no change in the percentage quantification of the YSZ phase when the bilayer number increased. For the Al_2O_3 phase, the percentage analysis of the phase indicated that there was a decrease as the interface number increased. This is attributed to structural percolation phenomena, because in the multilayer configuration, with values greater than $n = 1$ bilayer, the Al_2O_3 layer is located in an intermediate zone between the YSZ layer, which is the initial and the final layer of the multilayer

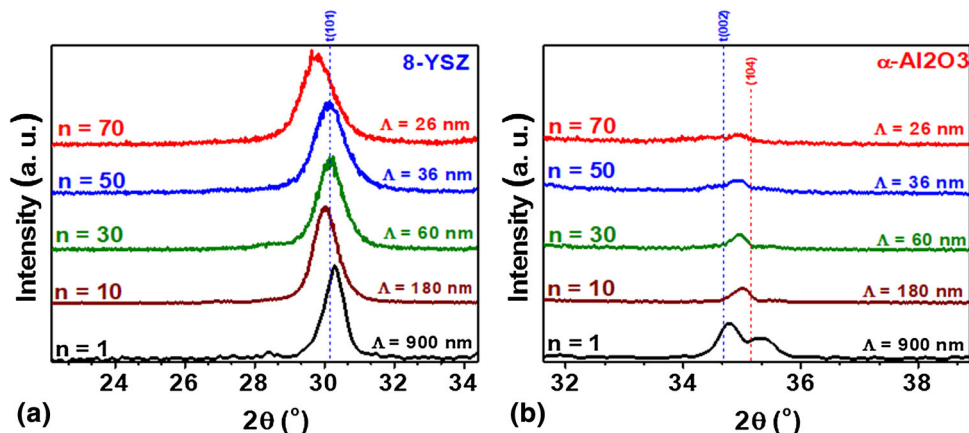


Fig. 3 Magnification of the highest intensity peaks $t(101)$ and (104) corresponding to 8YSZ and $\alpha\text{-Al}_2\text{O}_3$, respectively.

configuration of the coatings. This type of configuration induces a mechanical transformation of the phases due to structural stresses during the deposition process which increases with the bilayers number. Therefore, the development of the Al_2O_3 phase decreases.

3.2 Compositional Analysis

Figure 5(a) shows the SEM micrographs of the cross-section of the coating with $n = 1$ bilayer and a periodicity $\Lambda = 900$ nm, deposited on silicon substrates. A difference in the contrast for both layers can be observed, where the 8YSZ layer presents a bright contrast and the layer $\alpha\text{-Al}_2\text{O}_3$ presents a dark contrast. This difference, in contrast, is a characteristic attributed to the electron density of each layer. Figure 5(b) and (c) shows the EDX spectrum that determines the chemical composition of the layers and indicates that there was no other element that contaminated the layers during the deposition process or that could interfere with the behavior of the layers. Finally, Fig. 5(d) shows the SEM micrograph of the cross-section of the $[\text{8YSZ}/\alpha\text{-Al}_2\text{O}_3]_n$ coating with $n = 10$ bilayers ($\Lambda = 180$ nm), which determines that the system presented a multilayer design, with a homogeneous distribution in the thickness of each layer.

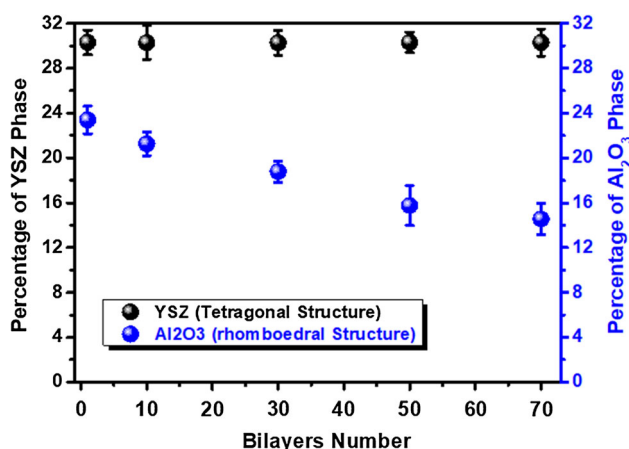


Fig. 4 Quantitative phase change relationship as a function of the bilayer number

3.3 Surface Analysis

Figure 6 presents the AFM images as a function of the bilayer number deposited on silicon substrates, where it was observed that the type of grain presented by the coatings was of a circular morphology. Also, it was determined that as the bilayer number increased, a greater homogeneity was generated on the surface of the coatings. These homogeneous surfaces are attributed to the high ionic bombardment of Ar^+ atoms during the deposition process. This modifies the coatings on the surface morphology due to the energy increase of the adsorbed atoms on the substrate surfaces, generating a higher number of nucleation sites (Ref 15, 16). These sites lead to a reduction in grain size and a decrease in the total roughness, as well as an increase in the density of the coatings (Ref 9, 17). Hence, a smooth and homogeneous surface is produced that reduces the susceptibility to corrosion when these coatings are exposed in aggressive environments (Ref 9).

Figure 7(a) and (b) shows the relationship of the surface roughness and the grain size of the $[\text{8YSZ}/\alpha\text{-Al}_2\text{O}_3]_n$ coatings as a function of the bilayer number. These allowed us to determine that by increasing the number of interfaces there was an approximate decrease of 58% in roughness and 30% in grain size when comparing the $n = 1$ bilayer ($\Lambda = 900$ nm) with the $n = 70$ bilayers ($\Lambda = 26$ nm). This behavior on the surface of the coating is attributed to the fact that by maintaining a constant thickness for all coatings and depositing a higher bilayer number (n) or interfaces, the grain growth is interrupted by the nucleation effects as a new layer is being deposited and restricts the growth of the previous layer. In this way, smaller grains and higher densities are obtained, generating a decrease in roughness (Ref 9).

3.4 Mechanical Properties

From the nanoindentation test and using the Oliver and Pharr method (Ref 17) on $[\text{8YSZ}/\alpha\text{-Al}_2\text{O}_3]$ multilayer coatings deposited on AISI 304 steel substrate, the hardness (H) (Fig. 8a), and the elastic modulus (E) (Fig. 8b) were obtained. Figure 7 shows the evolution of the mechanical properties, hardness, and the elastic modulus, as a function of the bilayer number (n). This behavior is related to the increase of interfaces or symmetry breaks while the total thickness of the coatings remains constant, since these interfaces act as impediments to the movement and generation of dislocations. In addition, physical factors such as the increased residual stress within the crystalline structure of the coatings (Fig. 3) and surface factors

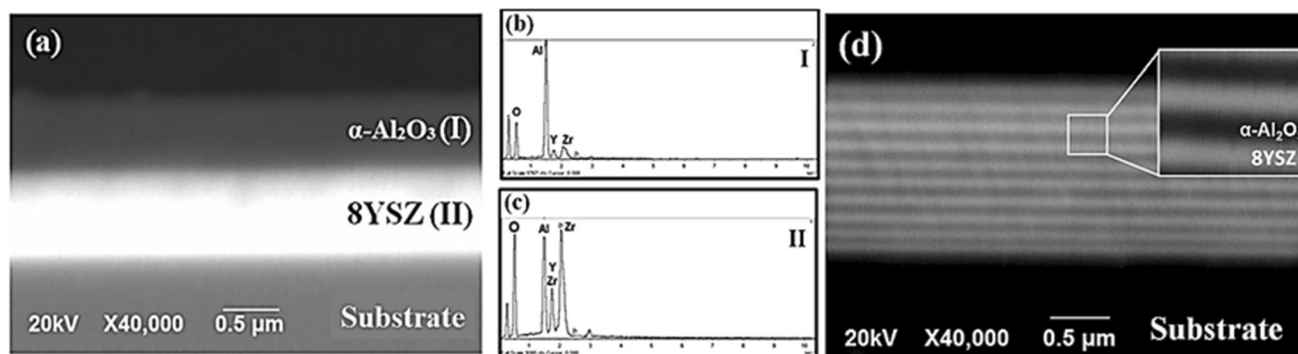


Fig. 5 SEM micrograph of the cross-section of the $[\text{8YSZ}/\text{Al}_2\text{O}_3]_n$ multilayer coating for (a) $n = 1$ bilayer ($\Lambda = 900$ nm) and (d) $n = 10$ bilayers ($\Lambda = 180$ nm) and EDX spectrum of (b) $\alpha\text{-Al}_2\text{O}_3$, and (c) 8YSZ

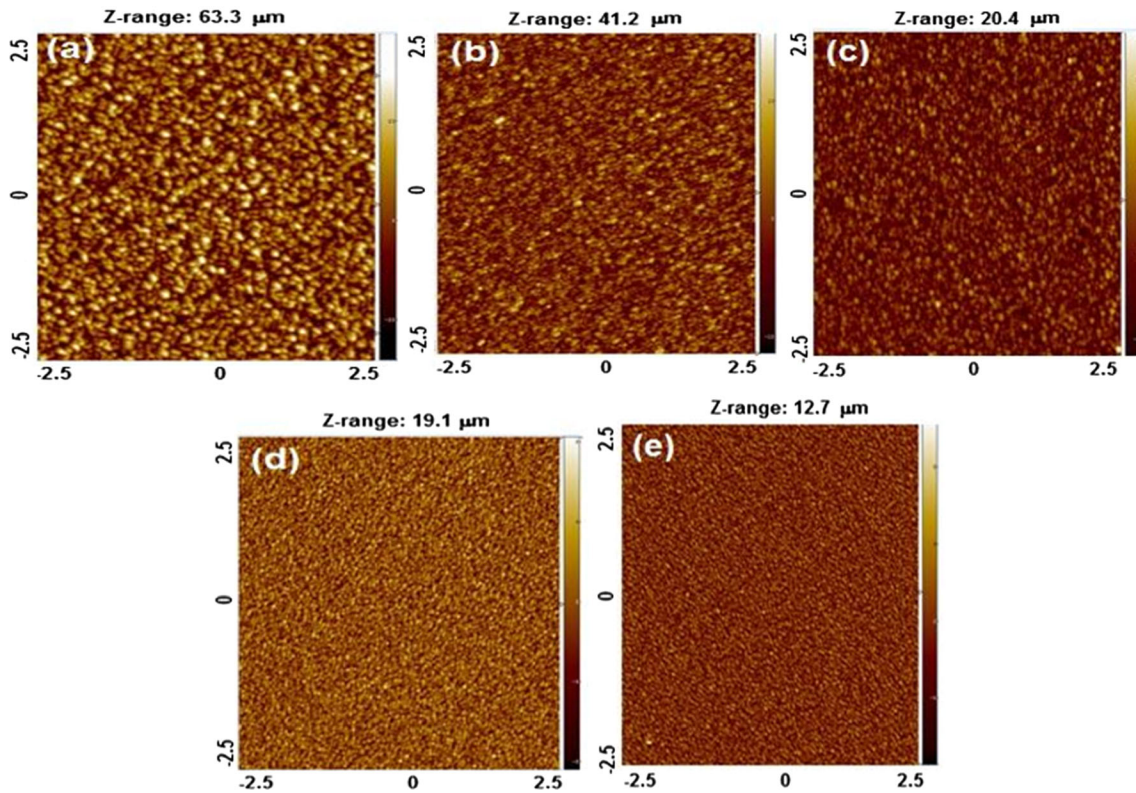


Fig. 6 AFM images of the $[8YSZ/\alpha-Al_2O_3]_n$ coatings as a function of the bilayer number (a) $n = 1$, (b) $n = 10$, (c) $n = 30$, (d) $n = 50$, and (e) $n = 70$

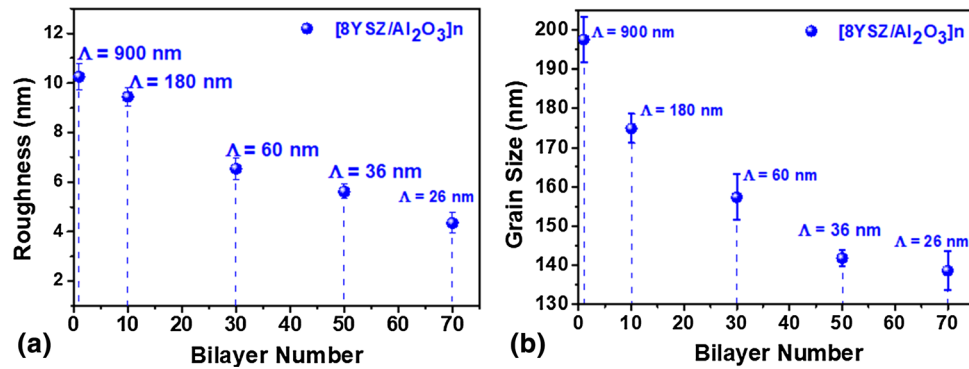


Fig. 7 Influence of the bilayer number on the surface morphology of the $[8YSZ/\alpha-Al_2O_3]_n$ coatings for (a) roughness and (b) grain size

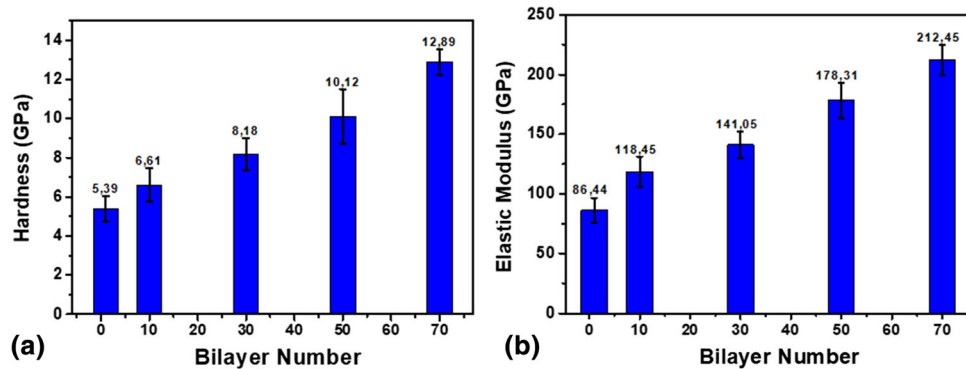


Fig. 8 Influence of the bilayers number on the mechanical properties of the $[8YSZ/\alpha-Al_2O_3]_n$ coatings for (a) hardness and (b) elastic modulus

such as grain size and roughness (Fig. 7), generate denser and more homogeneous coatings that influence the mechanical and tribological properties. Thus, the coating with 70 bilayers is able to withstand a higher external load applied on its surface relative to the other coatings (Ref 9, 18).

3.5 Adhesive Properties

The scratch test was used to characterize the adherence strength of the [8YSZ/ α -Al₂O₃]_n multilayer coatings as a function of the bilayers number deposited on the AISI 304 steel substrates. For this, the critical load (Lc2) was used, which is the load where the first delamination at the edge of the scratch track occurs (adhesive failure) (Ref 19, 20). One factor that impacts the critical load of a coating is the grain size, and when this decreases, the movement of inter-grain dislocations is impeded. Therefore, those dislocations will require a higher critical shear stress to move and propagate through the coating. Other important factors are the mechanical properties, such as hardness and elastic modulus. These surface characteristics define if a higher applied external load is required to penetrate the surface of the coating with 70 bilayers compared to the other. This is because of a higher number of interfaces or symmetry breaks at a constant thickness, which restricts the movement of dislocations through the layers. Finally, physical factors such as the internal stress within the crystal structure can improve the resistance of the coatings against crack propagation, thus preserving the integrity of the coatings under static and dynamic loads (Ref 20, 21).

3.6 Corrosion Analysis

To analyze the electrochemical behavior of the [8YSZ/ α -Al₂O₃]_n multilayer coatings as a function of the bilayer number ($n = 1, 10, 30, 50,$ and 70) deposited on AISI 304 steel substrate, the electrochemical impedance spectroscopy (EIS) technique was used. With this technique, the polarization resistance (R_p) values and electrochemical impedance values were obtained. To carry out this study through the EIS technique, an equivalent circuit was used which provided information related to the dissolution resistance, the polarization resistance, and the capacitance of the double layer (Ref 22). Generally, the equivalent circuit for TBCs coatings, obtained by deposition techniques such as APS and EB-PVD, consists in elements of an ideal capacitor. This is due to factors such as the surface roughness of the YSZ, the interfacial roughness of the junction layer, and the distribution of the pores, which generate frequency dispersion because the current density distribution is not uniform (Ref 22). However, in a low-dimensional system such as our study, the thicknesses of the top layer and the bonding layer are reduced, hence the pore size and surface roughness are on a nanometer scale, which significantly decreases the frequency dispersion of the system. Therefore, to identify the phases elements for the equivalent circuit of the multilayer coatings deposited using the magnetron sputtering r.f. technique, the results of the surface morphology obtained by the AFM technique were taken into account. There it was evidenced that these multilayer coatings presented surface homogeneity, higher density and lower total roughness with the increase of the bilayer number. Moreover, taking into account the low thickness of the [8YSZ/ α -Al₂O₃]_n coatings, it was possible to approximate the elements of the equivalent circuit to elements of a constant phase or CPE in this case named “ C_{cor} and C_c ”, to consider the two relaxation time constants. The

“ C_{cor} and R_{cor} ” elements predominate at high frequencies and are characteristic of the passive film formed or of the dielectric properties of the solution/coating interface. The Cc - Rpo pair, on the other hand, predominates at low frequencies and are particular to the corrosion process of the substrate/coating. Multilayer coatings can be approximated to the Randles cell circuit to simulate the phenomenon at the substrate/coating interface, which shows the double-layer capacitance in parallel with the impedance due to the transfer of ions from the electrolyte to the metallic substrate (Ref 22). The equivalent circuit model used with the constant phase elements to adjust the experimental data is shown in Fig. 10.

Once the equivalent circuit of the EIS technique was identified, the resulting electrochemical impedance values were used for the (Nyquist diagram). Figure 9 shows the Nyquist diagram of the uncoated steel substrate (AISI 304), and the [8YSZ/ α -Al₂O₃]_n multilayer coatings with the different bilayers number $n = 1, 10, 30, 50,$ and 70 . The diagram presents the imaginary impedance (Z_{imag}) versus real impedance (Z_{real}) in order to know the electrochemical response of the coatings immersed in the 3.5% NaCl + 0.5M-H₂SO₄ solution with suspended silica particles between 210 and 300 μ m. The Nyquist diagrams allowed to establish that there was a strong dependence of the circle arcs in relation to the increase of the bilayer number (n). This suggests that by increasing the number of layers that have a high resistance due to their ceramic nature at a constant thickness, the impedance will increase against degradation by corrosive-erosive phenomena.

Using the equivalent circuit (Eq. 1) and the Nyquist diagram (Fig. 10 and 11), it was possible to determine the values of polarization resistance (R_p).

$$Z_{RC} = -\frac{j\omega R_p^2 C}{R_p^2 \omega^2 C^2 + 1} + \frac{R_p}{\omega^2 R_p^2 C^2 + 1} + R_s \quad (\text{Eq 1})$$

where (ω) is the radial frequency, (R_p) polarization resistance, (R_s) solution resistance, and (c) Double-layer capacitance.

When evaluating Eq 1 at very low frequency values ($\omega = 0$), the first term of the equation is indeterminate, and since $R_s \ll R_p$, the polarization resistance (R_p) is approximately equal to Z_{RC} . The calculated polarization resistance (R_p) values are shown in Fig. 12. From this figure, it was observed that the R_p of the system tends to higher values as the bilayers number increased. This behavior of increasing R_p values is mainly attributed to the dense microstructure and homogeneous surface

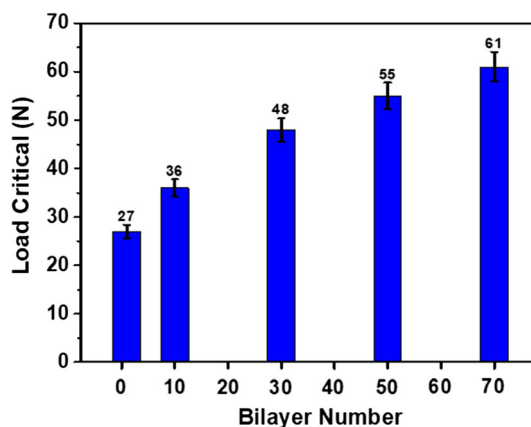


Fig. 9 Critical load (Lc2) as a function of the bilayer number

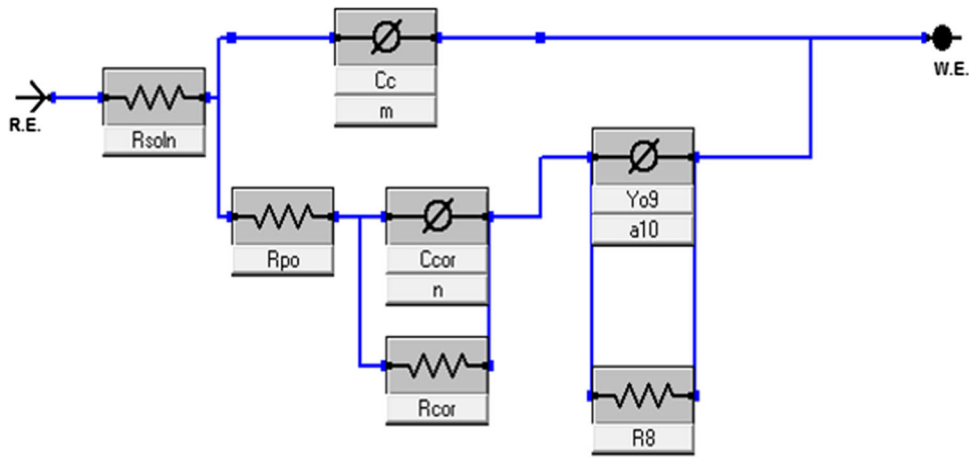


Fig. 10 Equivalent circuit used for fitting impedance data for the $[8YSZ/\alpha-Al_2O_3]_n$ coatings. (RE) reference electrode, (R_{soln}) electrolytic resistance, (R_{corr}) resistance between solution and coatings, (R_{po}) polarization resistance, (C_{cor}) capacitance between solution and coating, (n) exponential coefficient (CPE-Ccor exponent), (C_c) capacitance between coating and metal (Cdl), (m) exponential coefficient (CPE-Cc coefficient), (WE) working electrode

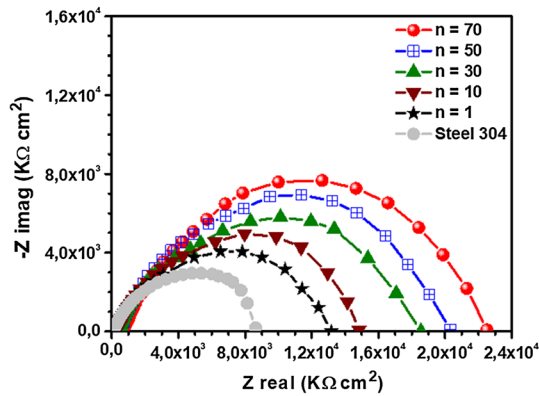


Fig. 11 Nyquist diagram of the uncoated steel (AISI 304) and the $[8YSZ/\alpha-Al_2O_3]_n$ coatings as a function of the number of bilayers $n = 1, 10, 30, 50,$ and 70

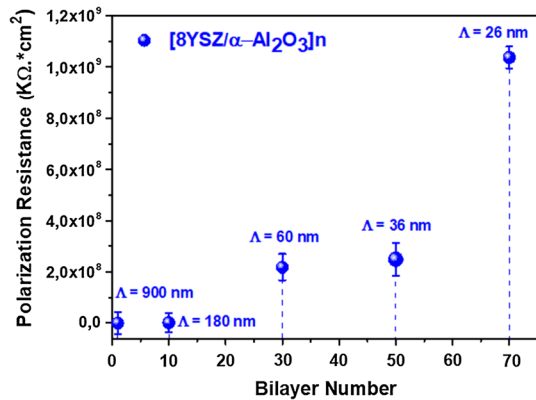


Fig. 12 Polarization resistance of the $[8YSZ/\alpha-Al_2O_3]_n$ coatings as a function of the bilayers number

of the $[8YSZ/\alpha-Al_2O_3]_n$ coatings. These characteristics inhibit the electrolyte to embed inside the coating, as well as through the thickness of the coatings which are of low dimensionality. Moreover, for the multilayer systems with the highest number of interfaces ($n = 70$ bilayers), the interfaces work as obstacles

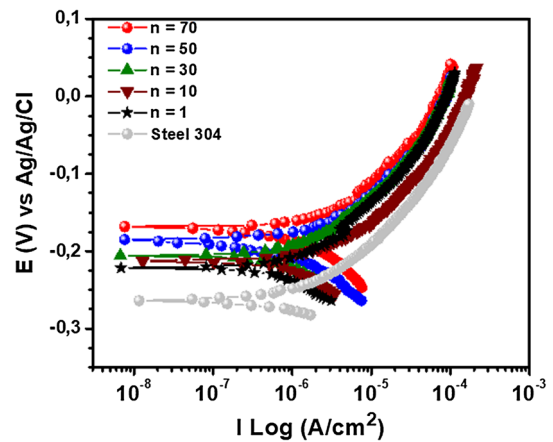


Fig. 13 Tafel polarization curves of the 304 steel substrate and the $[8YSZ/\alpha-Al_2O_3]_n$ coatings, $n = 1, 10, 30, 50,$ and 70 , subjected to corrosive conditions

to the movement of the chloride ions (Cl^-) towards the substrate. Thus, the $[8YSZ/\alpha-Al_2O_3]_{70}$ coatings produced the highest protection relative to the coating with the lowest number of interfaces or bilayers number ($n = 1, \Lambda = 900$ nm).

To obtain more information about the electrochemical behavior of the material, polarization curves (Fig. 13) were made of the multilayer coatings under corrosion-erosion conditions by plotting corrosion potential as a function of the current density. The parameters found in the polarization curves (anodic and cathodic slopes) allowed to make use of the Stern-Gearry equation to find the corrosion current densities and corrosion rates of the multilayer coatings.

Figure 13 compares the polarization curves of all the multilayer coatings and the uncoated steel substrate (AISI 304). From these results, it was possible to determine that as the bilayer number (n) increased and the bilayer period (Λ) decreased, the curves shifted to lower current densities and higher current potentials. This behavior is attributed to the changes in the electronic potential by the effect of the interfaces, which reduce the possibility of the Cl^- ions to migrate freely towards the substrate surface, increasing the

electrochemical potential and improving the corrosion–erosion resistance. Using the results obtained through the EIS technique and Tafel polarization curves, it was possible to calculate the variables of the electrochemical behavior such as the corrosion rate, the porosity factor, and the efficiency of the bilayers number (n). From the Stern–Geary equation (Eq. 2, 3) the current intensity and the corrosion rate were calculated.

$$I_{\text{corr}} = \frac{\beta_a \beta_c}{2.303 R_p (\beta_a + \beta_c)} \quad (\text{Eq 2})$$

$$\text{Rate Corrosion} = \frac{I_{\text{corr}} * K * E_w}{d} \quad (\text{Eq 3})$$

The polarization resistance increased as the bilayer number also increased and was inversely proportional to the corrosion rate, as corroborated in Fig. 14. This behavior is attributed to the action of the corrosive–erosive mechanisms occurring in the coatings during the electrochemical test, since this test generates a generalized corrosion phenomenon, and the passive film formed on the surface is eliminated and removed by the action of the wear particles. These mechanisms act cooperatively and lead to the loss of protection against corrosion and erosive wear.

On the other hand, the relationship of the corrosion rate values with respect to the bilayers number was inversely proportional, due to how the reaction kinetics of the corrosive–erosive mechanisms developed. This was caused by the increase in the interfaces or bilayers number which presented relevant changes in the crystallographic orientation and/or symmetry breaks. Therefore, these interfaces acted as dispersion points that prevented the propagation of the electrolyte towards the substrate, thus the generation of the passive layer was lower in relation to the coating with the lowest bilayer number. From these results, it was also possible to determine that the structural integrity of the coatings was higher as the bilayers number increased (Ref 23, 24).

The porosity factor versus the electrochemical flux (layer porosity percentage) corresponds to the relationship between the polarization resistance of the uncoated substrate and the substrate coated with the multilayers, as shown by the following equation.

$$P = \frac{R_{p,u}}{R_{p,r-u}} \quad (\text{Eq 4})$$

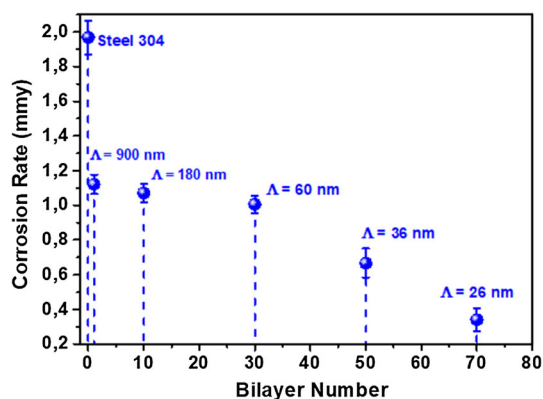


Fig. 14 Corrosion rate of the steel substrate (AISI 304) and the [8YSZ/ α -Al₂O₃]_n multilayer coatings as a function of the bilayers number

where P is the porosity of the total coating, $R_{p,u}$ in the polarization resistance of the uncoated substrate and $R_{p,r-u}$ is the polarization resistance of the coating.

The values calculated from Eq. 4 are shown in Fig. 15. From these results, it was determined that the efficiency of the coating with the highest bilayer number ($n = 70$ bilayers) against the corrosive test with suspended solid particles presented an increase of 82.7% with respect to the uncoated substrate. This can be attributed to the decrease in current density during the corrosive process, since, as shown in the Tafel polarization curves, as the bilayers number increases the current density decreased. This shows that the electrochemical properties of the coating improve as a function of the bilayer number.

The protection efficiency of the [8YSZ/ α -Al₂O₃]_n multilayer coatings was calculated by Eq. 5 (Ref 25).

$$E_f(\%) = \left(\frac{I_{\text{corrs}} - I_{\text{corrf}}}{I_{\text{corrs}}} \right) \quad (\text{Eq 5})$$

where I_{corrs} is the corrosion current of the substrate and I_{corrf} is the corrosion current of the coatings.

3.7 Surface Analysis of the Coatings after the Corrosive–Erosive Test with Suspended Solids

To observe the surface degradation caused by the electrochemical test (Tafel and EIS) on the steel substrate (AISI 304) and the [8YSZ/ α -Al₂O₃]_n multilayer coatings, the surfaces were analyzed by optical microscopy. A change of tonality or different contrasts was evidenced, a light contrast due to the reflectivity of the steel and a dark tonality due to the presence of the coating on the surfaces. Figure 16(a) shows the optical microscopy on the uncoated steel, where it can be seen that there was a dark tonality in the external areas of the surface, belonging to the oxides present which were generated during the electrochemical test. From Fig. 16(b)–(e), it was determined that as the bilayer number increased, the light zone (exposed steel) decreased considerably. This indicated that there was less removal or degradation of the coating during the corrosion with suspended solid particles test, meaning that a higher bilayer number ($n = 70$ bilayers) generates a greater impediment to the passage of Cl⁻ ions present in the electrolyte and a less erosive wear.

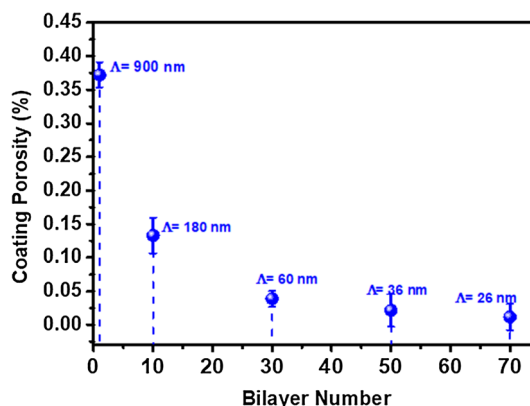


Fig. 15 Efficiency of the [8YSZ/ α -Al₂O₃]_n multilayer coating as a function of the bilayers number $n = 1, 10, 30, 50,$ and 70

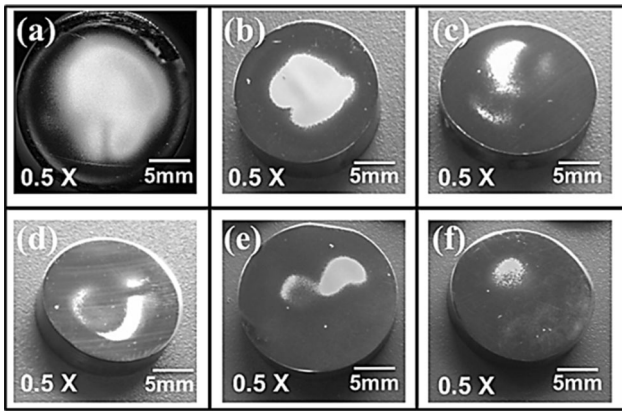


Fig. 16 Optical microscopy images after the corrosion–erosion test of the (a) Steel substrate (AISI 304) and the coatings with (b) $n = 1$ bilayer, (c) $n = 10$ bilayers, (d) $n = 30$, (e) $n = 50$ bilayers, and (f) $n = 70$ bilayers

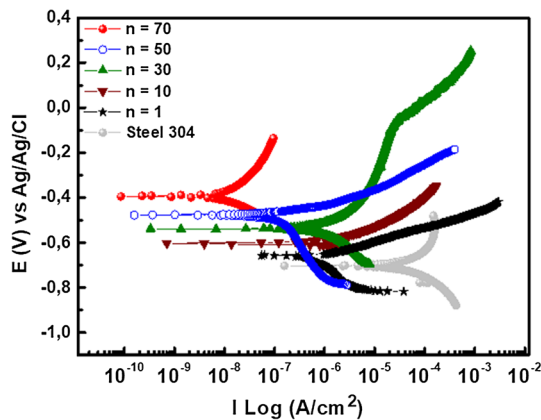


Fig. 17 Tafel curves of corrosion–erosion for the $[8YSZ/\alpha-Al_2O_3]_n$ multilayer coatings as a function of bilayer number

3.8 Corrosion Analysis with Erosive Effect

Figure 17 shows the Tafel polarization curves using the tribometer of the corrosive–erosive test as illustrated previously in Fig. 1. These Tafel curves allowed to determine the values of the anodic and cathodic slopes. From these results, a passive behavior was observed in all the samples analyzed. This was attributed to the fact that the coatings generated a displacement of the curves towards lower values of current density and nobler potentials compared to that of the uncoated substrate. This behavior is related to the increase in the bilayers number (n), evidencing that a higher interface number and a shorter period of bilayers in multilayer coatings improve the response against corrosive–erosive effects (Ref 26).

Figure 18 shows the values of corrosion rate as a function of bilayers number (n) and bilayers period (Δ) when subjected to in corrosive–erosive environments using the tribometer as illustrated in Fig. 1. These curves presented a trend towards lower values as the bilayer number increased and the bilayer period decreases. These types of coatings generate a higher number of interfaces such as those shown by SEM results, which are regions that present structural disorder and mark changes in the crystallographic orientation. These interfaces can act as dispersion points preventing the electrolyte from

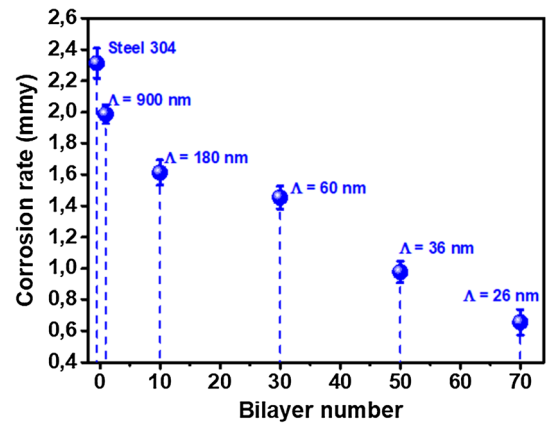


Fig. 18 Corrosion rate of the $[8YSZ/\alpha-Al_2O_3]_n$ multilayer coatings as a function of the bilayer number when exposed to corrosion–erosion test

spreading towards the substrate, which causes damage to the surface (Ref 27). Figure 18 shows a higher corrosion rate when the surface of the coatings is under an angle of 90° in relation to the corrosion rate in an environment with suspended solids. This phenomenon is due to the high energy particles impacting the surface causing significant wear on the structural integrity of the coating. In that sense, it was found that the coating deposited with $n = 70$ ($\Delta = 26$ nm) under an impact angle of 90° provides a lower corrosion rate. This was due to the increased interface number and the bilayer period (Δ) reduced.

3.9 Analysis of Surface Degradation by Scanning Electron Microscopy (SEM and EDX) After the Corrosion–Erosion Test

In order to study in more detail, the surface damage on the multilayer coatings subjected to the corrosion–erosion environment as illustrated in Fig. 1, the scanning electron microscopy (SEM) and energy-dispersive x-ray spectroscopy (EDX) techniques were used on the surface of the coatings in order to study their surface after the corrosion–erosion test. By means of the electron density of the materials and the contrast changes (gray scale), it was possible to identify the wear zones or degraded zones of the coating. In addition, the elemental chemical composition of these zones is presented in Fig. 19, 20, 21, 22, and 23 and was determined by EDS. From these results, three distinct topographic areas or zones were identified, the non-degraded coating zone represented by a dark tonality (zone I), in these conditions, it is defined as the “superficial” continuity and continuity of color in the gray scale of the coating; an intermediate area corresponding to zone II, which represents the disturbed coating in its structural continuity and finally the exposed substrate (zone III) in this zone, there is a complete delamination of the coating due to the Kinect energy associated with the constant impact of the abrasive particles during the test. Thus, the structural integrity of the coating is affected leaving the substrate (AISI 304 steel) exposed.

Figure 19, 20, 21, 22, and 23 presents the surfaces and compositional analyses according to the zones mentioned above, Fig. 19(a), 20, 21, 22, and 23(a) presents the SEM micrograph of the degraded surfaces, where the three characteristic stages were evidenced. In addition, cracks were observed in the intermediate zone (zone II) between the coating and the exposed steel. These cracks were generated by the

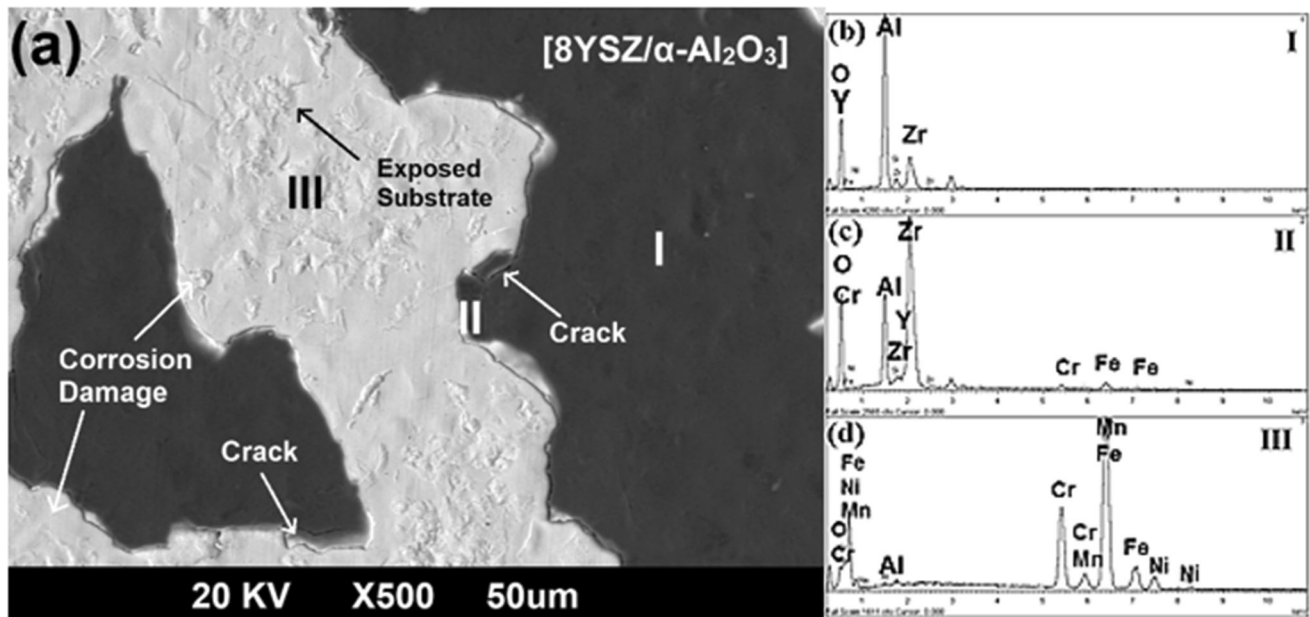


Fig. 19 $[8\text{YSZ}/\alpha\text{-Al}_2\text{O}_3]_n$ coating with $n = 1$ bilayer (a) SEM surface micrograph 500 \times , (b) EDX spectrum of the coating (zone I), (c) EDX spectrum of intermediate area (zone II), and (d) EDX spectrum of the exposed substrate (zone III)

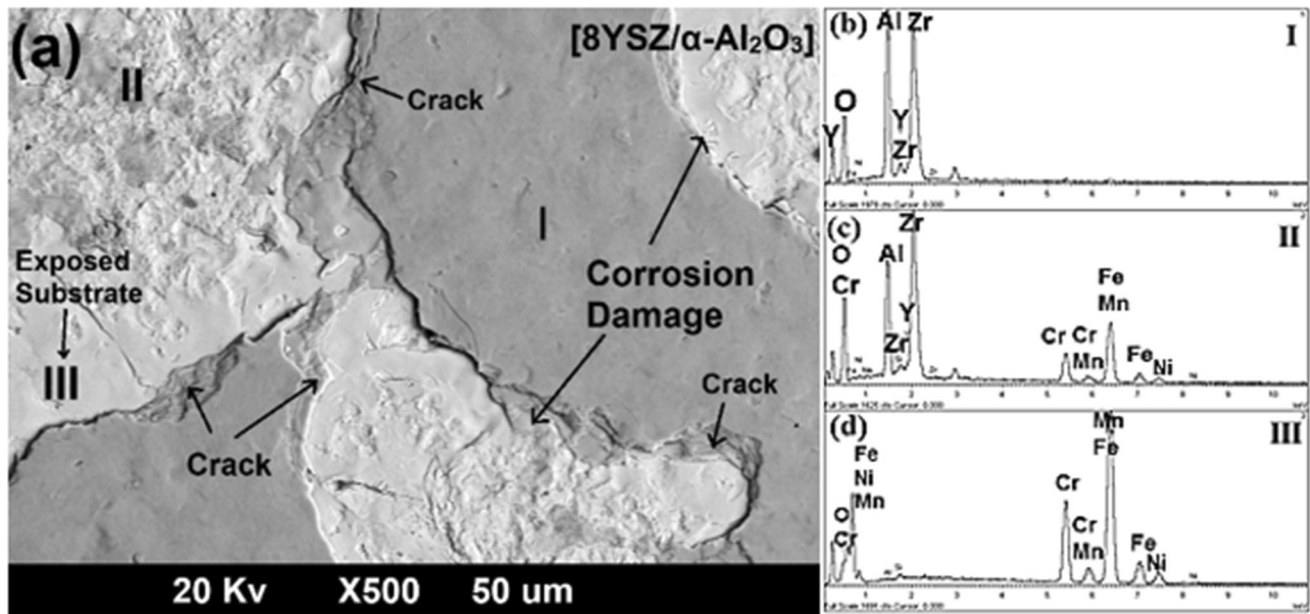


Fig. 20 $[8\text{YSZ}/\alpha\text{-Al}_2\text{O}_3]_n$ coating with $n = 10$ bilayer (a) SEM surface micrograph 500 \times , (b) EDX spectrum of the coating (zone I), (c) EDX spectrum of intermediate area (zone II), and (d) EDX spectrum of the exposed substrate (zone III)

kinetic energy of the silica particles that impacted the surface under a normal angle of (90°), causing a detachment of the coating. Also, in zone III (exposed steel), the presence of surface wear generated by the silica particles that were highly erosive was evidenced; however, there was no evidence of erosive wear in zone I (coating), thus demonstrating the contribution of the multilayer coatings to the corrosive-erosive wear resistance. From these zones (I, II and III), it was possible to show a relationship between the areas according to the bilayer number, mainly with zones I and III, attributed to the coatings and the exposed steel, respectively. By means of the

area ratio analysis, it was determined that the coatings with the highest bilayers number ($n = 70$ bilayers) presented a greater conservation of its structural integrity, in other words, it preserved a higher area of zone I in relation to the other surfaces, after the corro-erosive test. This behavior is due to physical factors such a higher bilayer number which influenced in the improved surfaces, mechanical and adhesive properties (Fig. 7, 8 and 9), hence, this coating was able to withstand the impact of the abrasive particles.

In addition, Fig. 19, 20, 21, 22, and 23 shows the EDX spectrum of the zone I, II and III. From these results, it was

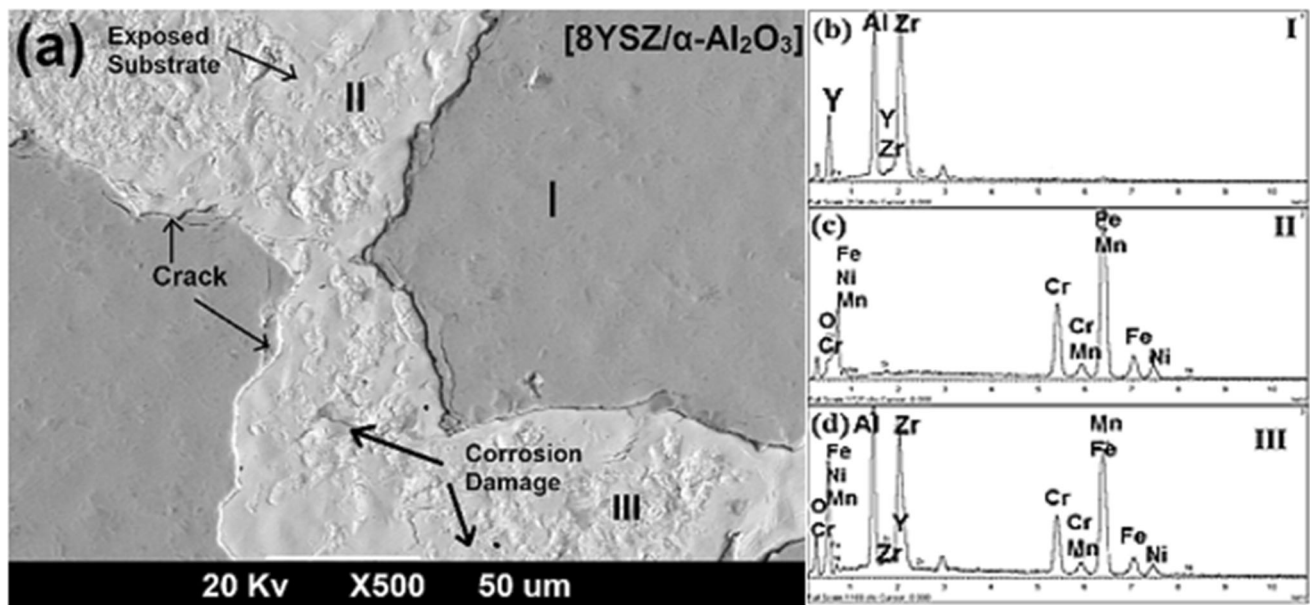


Fig. 21 $[8\text{YSZ}/\alpha\text{-Al}_2\text{O}_3]_n$ coating with $n = 30$ bilayer (a) SEM surface micrograph 500 \times , (b) EDX spectrum of the coating (zone I), (c) EDX spectrum of intermediate area (zone II), and (d) EDX spectrum of the exposed substrate (zone III)

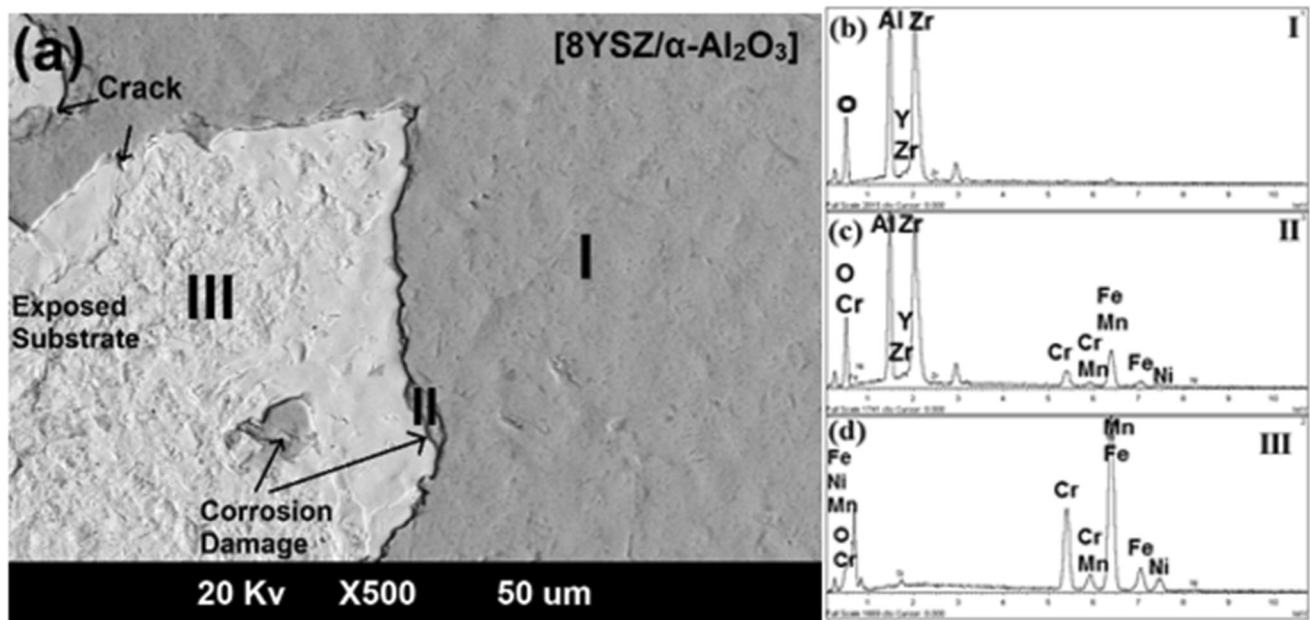


Fig. 22 $[8\text{YSZ}/\alpha\text{-Al}_2\text{O}_3]_n$ coating with $n = 50$ bilayer (a) SEM surface micrograph 500 \times , (b) EDX spectrum of the coating (zone I), (c) EDX spectrum of intermediate area (zone II) and (d) EDX spectrum of the exposed substrate (zone III)

determined that zone I, only presented elements corresponding to the coating (Al, O, Y, Zr) and no elements characteristic of the substrate were found. Thus, it is corroborated that in zone I the coating still contained its structural integrity. The spectrum of the intermediate zone (zone II) showed that there were elements of the coating (Al, O, Y, Zr) but also presents elements characteristic of the substrate (Cr, Fe). The presence of these elements is due to the degradation and fracture of the coating leaving part of the substrate exposed. Finally, zone III showed the presence of other elements such as (Ni, Mn, Cr, Fe), which are characteristic of the substrates.

3.10 Loss Mass Analysis After Corrosive–Erosive Test

To quantify the corro-erosion study presented above, the mass loss was analyzed as shown in Fig. 24. The synergistic effect generated by the corrosion–erosion mechanisms during the tribological test (Fig. 1) was produced by the kinetic energy associated with the impact of the abrasive particles on the coating surfaces, which caused fractures and delamination of the coating. Thus, through the mass loss, it was determined that the coating presented a lower wear during the test (Ref 28).

The total mass loss due to corrosion–erosion was calculated from the following equation (Ref 28).

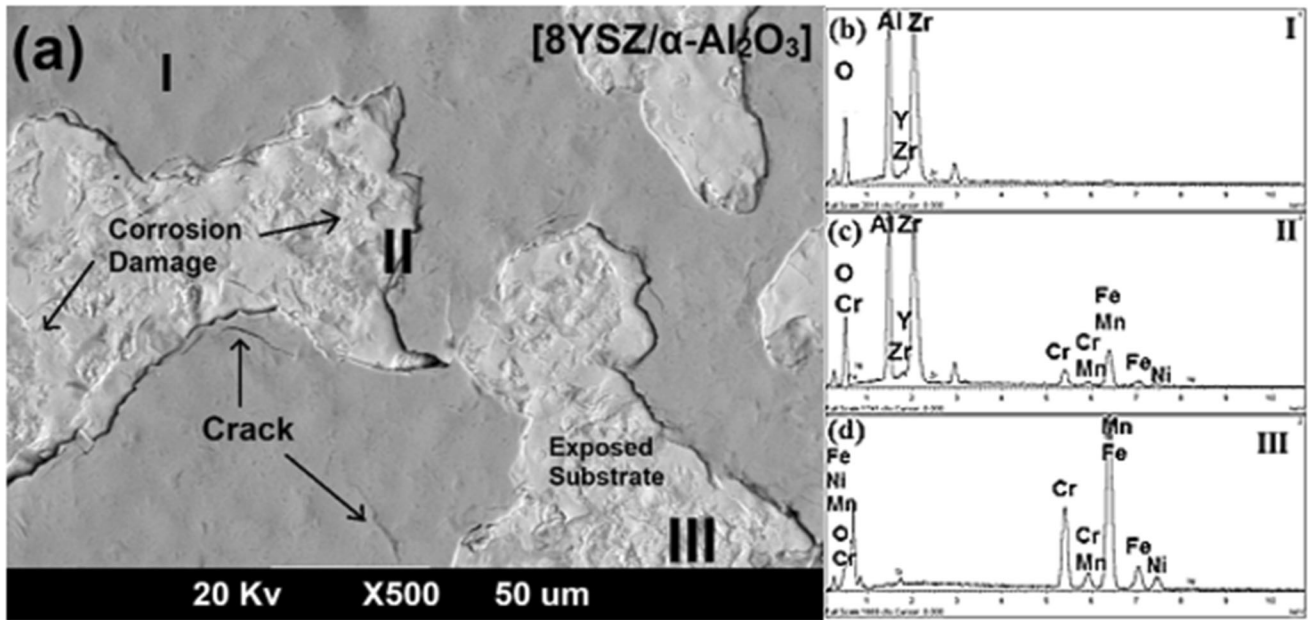


Fig. 23 $[8\text{YSZ}/\alpha\text{-Al}_2\text{O}_3]_n$ coating with $n = 70$ bilayer (a) SEM surface micrograph 500 \times , (b) EDX spectrum of the coating (zone I), (c) EDX spectrum of intermediate area (zone II) and (d) EDX spectrum of the exposed substrate (zone III)

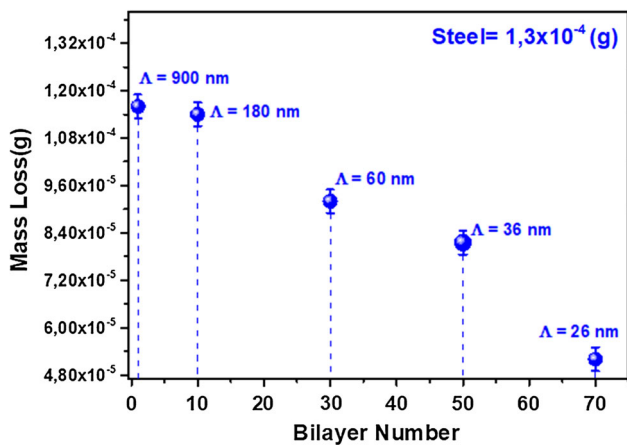


Fig. 24 Mass loss of all $[8\text{YSZ}/\alpha\text{-Al}_2\text{O}_3]_n$ multilayers coatings after corrosive-erosive test

$$\text{TWL} = E + C + S \quad (\text{Eq 6})$$

Total mass loss for additive and synergistic effects

$$\text{TWL}: E + E_0 + \Delta C_E + \Delta E_C \quad (\text{Eq 7})$$

$$\Delta E_S = S \wedge C = C_0 + \Delta C_e \quad (\text{Eq 8})$$

$$C = \frac{i \times W \times A \times T}{F \times n} \quad (\text{Eq 9})$$

where (TWL) is corrosion-erosion mass loss; (E) erosion loss; (C) electrochemical corrosion loss during the erosion; (C_0) electrochemical corrosion loss in a dynamic environment; (ΔE_S) additive effect in the corrosion-erosion; (S) synergistic

effect in the corrosion-erosion; (i) current density ($\mu\text{A}/\text{cm}^2$); (w) atomic weight (g/mol); (A) exposure area (cm^2); (T) exposure time; (F) faraday constant ($96,500 \text{ C}/\text{mol}$) and (n) ions number.

Figure 24 presents the mass loss as a function of the bilayer number. During this study, it was observed that the wear was related to the aggressive effect of the medium, since the chloride ion attack promoted the phenomenon of localized corrosion, which can advance through the substrate without the need to expand the affected zones and the amount of electrolyte is reduced. Therefore, it could be assumed that the wear micro-mechanisms (localized corrosion and impact of wear particles) were responsible for the corrosion progress favoring further removal of the external layers of the multilayers. Thus, it was determined that the multilayer systems with the highest bilayers number (70 bilayers) has the lowest amount of mass loss. This behavior is attributed to the physical and electrochemical properties of the surface, since a higher bilayers or interfaces number leads to a dissipation of corrosive ions when the surface is attacked. In addition, the structural (compressive stresses), morphological (lower roughness and smaller grain size), mechanical (hardness and elastic modulus), and tribological (adhesion strength) properties of this surface (70 bilayers), gave this coating the properties with it was able to withstand the kinetic energy of the impact generated by the abrasive particles during the corro-erosive test, making it the best candidate to be implemented in corro-erosive environments.

3.11 Merit Index

Figure 25 and 26 presents the merit index obtained through this study with the objective to determine which coating presented the best set of properties as shown by the dotted lines. Figure 25 shows the direct relationship between the mass loss and the corrosion rate of all surfaces studied. With this analysis, it was determined that the coating with the highest bilayer

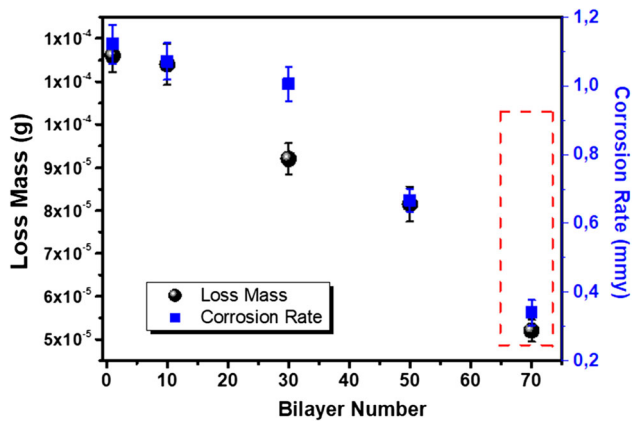


Fig. 25 Merit index between the mass loss and the corrosion rate as a function of bilayers number (n) of the $[8YSZ/\alpha-Al_2O_3]_n$ multilayers coatings

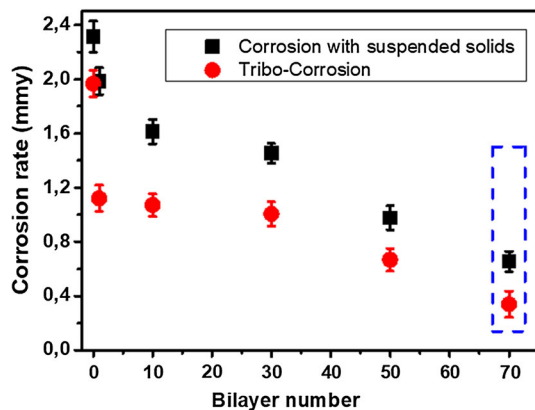


Fig. 26 Correlation of the corrosion rate in environments corrosive and tribo-corrosive environments of the coatings as a function of the bilayer number (n)

number (70 bilayers) presented a lower mass loss and lower corrosion rate during the electrochemical test. This behavior is attributed to the higher number of interfaces, which were able to withstand the kinetic energy associated with the impact of the abrasive particle during the corro-erosive test. In addition, this higher number of interfaces restricted the passage of the Cl^- ion present in the electrolyte towards the substrate. Therefore, the coating with 70 bilayers presents the best corrosion resistance and the best ability to withstand the impact of the abrasive particles on the surface.

Figure 26 presents a comparison of the behavior of the multilayer coatings when subjected to an electrochemical study with suspended solids and tribo-corrosive as illustrated in Fig. 1. From these results, it was concluded that the coating with 70 bilayers also presented the best set of properties. This is because a higher bilayer number is able to withstand the external energy associated with the impact of the abrasive particles. Thus, the structural integrity of the coating was maintained for a longer time in relation to the coatings with a lower bilayers number, causing a lower corrosion rate. Therefore, it was determined that the coating with 70 bilayers presented the best set of properties and is the ideal candidate to be implemented as a protective coating against the corrosive and corro-erosive environments.

4. Conclusion

Electrochemical test determined that the coating with $n = 70$ bilayers presented a 58.5% reduction in the corrosion rate in relation to the coating with $n = 1$ bilayer. This behavior is attributed to the increase in the number of interfaces or bilayers, which generates a higher impediment to the passage of Cl^- ions present in the electrolyte to the substrate. In addition, the coating with 70 bilayers showed a lower roughness, which inhibits the inclusion of the electrolyte in the surface areas of the coating.

Through the morphological study, a decrease of approximately 58% and 30% for roughness and grain size, respectively when comparing the $n = 1$ bilayer ($\Lambda = 900$ nm) with the $n = 70$ bilayers ($\Lambda = 26$ nm) was determined. This behavior is attributed to the fact that by maintaining a constant thickness for all coatings and depositing a higher bilayers number (n) or interfaces, grain growth is interrupted by nucleation effects, since depositing a new layer restricts the growth of the previous layer. In addition, structural factors such as the presence of compressive stresses cause a denser and more compact structure, resulting in smaller grain sizes.

From the corrosive-erosion study of the coatings, the wear or surface degradation of the coatings was evidenced due to the high impact of the abrasive particles during the corro-erosive test, determining fracture zone on each surface and localized corrosion zone due to the loss of protection of the coating. Finally, this wear was calculated by mass loss, obtaining a decrease of 77.73% when comparing the 50 bilayers coating with the 1 bilayer coating, which corroborated by the protective effect of the 50 bilayers coating under corrosive-erosive conditions.

It was found that the coating with $n = 70$ bilayers showed a lower surface degradation of the coating. Thus, it can be concluded that the coating with the highest interfaces number has the best electrochemical properties, as well as a higher resistance to the corrosive-erosive systems, being this multilayer coating is the best option to be chosen as a protective coating on devices or parts exposed to highly aggressive environments.

Acknowledgments

This research was supported by the Tribology, Polymers, Powder Metallurgy and Solid Waste Transformations research group of the Universidad del Valle; Recubrimientos Duros y Aplicaciones Industriales (RDAI) research laboratory of the Universidad del Valle; And the “Universidad Militar Nueva Granada” under contract IPM ING 3123 Validity 2020-2021,

References

1. A. Feuerstein, J. Knapp, T. Taylor, A. Ashary, A. Bolcavage and N. Hitchman, Technical and Economical Aspects of Current Thermal Barrier Coating Systems for Gas Turbine Engines By Thermal Spray and EBPVD: A Review, *J. Therm. Spray Technol.*, 2008, **17**(2), p 199–213. <https://doi.org/10.1007/s11666-007-9148-y>
2. A. Escarraga, A. Toro, Y. Aguilar, J.C. Caicedo and G. Zambrano, Thermal Cyclic Response of $[8YSZ/Al_2O_3]_n$ Multilayered Coatings Deposited Onto AISI 304 Stainless Steel, *Mater. Chem. Phys.*, 2018, **216**, p 526–533. <https://doi.org/10.1016/j.matchemphys.2018.05.039>

3. A.G. González, F.M. Hurtado, H. Ageorges, E. López and F. Vargas, Evaluación del Comportamiento a la Corrosión en Sales Fundidas de Recubrimientos de Circona Estabilizada con Itria Elaborados por Proyección Termica por Plasma Atmosférico, *Rev. Latinoam. Metal. y Mater.*, 2017, **37**(1), p 2–10.
4. V. Kumar and K. Balasubramanian, Progress Update on Failure Mechanisms of Advanced Thermal Barrier Coatings: A Review, *Prog. Org. Coatings*, 2016, **90**, p 54–82. <https://doi.org/10.1016/j.porgcoat.2015.09.019>
5. G. Moskal, The Porosity Assessment of Thermal Barrier Coatings Obtained by APS Method, *J. Achiev. Mater. Manuf. Eng. JAMME*, 2007, **20**(1–2), p 483–486. <https://doi.org/10.1007/s00394-015-0886-1>
6. B. Saruhan, U. Schulz and M. Bartsch, Developments in Processing of Ceramic Top Coats of EB-PVD Thermal Barrier Coatings, *Key Eng. Mater.*, 2007, **333**, p 137–146. <https://doi.org/10.4028/0-87849-424-3.137>
7. F. Blas et al., Processing Thermal Barrier Coatings Via Sol–Gel Route: Crack Network Control and Durability, *Surf. Coatings Technol.*, 2017 <https://doi.org/10.1016/j.surfcoat.2017.11.008>
8. D.G. Cahill et al., Nanoscale Thermal Transport, *J. Appl. Phys.*, 2003, **93**(2), p 793–818. <https://doi.org/10.1063/1.1524305>
9. C.H. Ortiz, H.D. Colorado, W. Aperador and A. Jurado, Influence of the Number of Bilayers on the Mechanical and Tribological Properties in $[\text{TiN}/\text{TiCrN}]_n$ Multilayer Coatings Deposited by Magnetron Sputtering, *Tribol. Ind.*, 2019, **41**(3), p 330–343. <https://doi.org/10.24874/ti.2019.41.03.03>
10. C. Zhu, A. Javed, P. Li, F. Yang, G.Y. Liang and P. Xiao, A Study of the Microstructure and Oxidation Behavior of Alumina/Yttria-Stabilized Zirconia ($\text{Al}_2\text{O}_3/\text{YSZ}$) Thermal Barrier Coatings, *Surf. Coatings Technol.*, 2012, **212**, p 214–222. <https://doi.org/10.1016/j.surfcoat.2012.09.052>
11. G. Venkadesan and J. Muthusamy, Experimental Investigation of $\text{Al}_2\text{O}_3/8\text{YSZ}$ and $\text{CeO}_2/8\text{YSZ}$ Plasma Sprayed Thermal Barrier Coating on Diesel Engine, *Ceram. Int.*, 2019, **45**(3), p 3166–3176. <https://doi.org/10.1016/j.ceramint.2018.10.218>
12. C. Amaya et al., Corrosion Study of Alumina/Yttria-Stabilized Zirconia ($\text{Al}_2\text{O}_3/\text{YSZ}$) Nanostructured Thermal Barrier Coatings (TBC) Exposed to High Temperature Treatment, *Corros. Sci.*, 2009, **51**, p 2994.
13. K. He, J.J. Chen, W.X. Weng, C.C. Li and Q. Li, Microstructure and Mechanical Properties of Plasma Sprayed Al_2O_3 -YSZ Composite Coatings, *Vacuum*, 2018, **151**, p 209–220. <https://doi.org/10.1016/j.vacuum.2018.01.038>
14. M.J. Kelly, D.E. Wolfé, J. Singh, J. Eldridge, D.M. Zhu and R. Miller, Thermal Barrier Coatings Design with Increased Reflectivity and Lower Thermal Conductivity for High-Temperature Turbine Applications, *Int. J. Appl. Ceram. Technol.*, 2006, **3**(2), p 81–93. <https://doi.org/10.1111/j.1744-7402.2006.02073.x>
15. C. Amaya et al., Influence of Bias Voltage on the Crystallographic Orientation and Morphology of Sputter Deposited Yttria Stabilized Zirconia (YSZ) Thin Films, *Phys. status solidi*, 2007, **4**, p 4288–4293. <https://doi.org/10.1002/pssc.200675925>
16. G. De Películas, D. Universidad, Estudio del Comportamiento Tribológico y Adhesivo de Multicapas de $[\text{Al}_2\text{O}_3/\text{YSZ}]$ 2006, **1**(1), p 1–6
17. L. Ipaz, J.C. Caicedo, J. Esteve, F.J. Espinoza-Beltran and G. Zambrano, Improvement of Mechanical and Tribological Properties in Steel Surfaces by Using Titanium–Aluminum/Titanium–Aluminum Nitride Multilayered System, *Appl. Surf. Sci.*, 2012, **258**(8), p 3805–3814. <https://doi.org/10.1016/j.apsusc.2011.12.033>
18. I.A. Mahmood, W.W. Jameel and L.A. Khaleel, Improved Oxidation Resistance for Thermal Barrier Ceramic Coating Protect, *Int. J. Res. Eng. Technol. (IMPACT IJRET)*, 2013, **1**(5), p 77–86.
19. S. Vepřek and S. Reiprich, A Concept for the Design of Novel Superhard Coatings, *Thin Solid Films*, 1995, **268**(1–2), p 64–71. [https://doi.org/10.1016/0040-6090\(95\)06695-0](https://doi.org/10.1016/0040-6090(95)06695-0)
20. B. Podgornik, S. Hogmark, O. Sandberg and V. Leskovsek, Wear Resistance and Anti-sticking Properties of Duplex-treated Forming Tool Steel, *Wear*, 2003, **254**(11), p 1113–1121. [https://doi.org/10.1016/S0043-1648\(03\)00322-3](https://doi.org/10.1016/S0043-1648(03)00322-3)
21. K. Holmberg, H. Ronkainen and A. Matthews, Tribology of Thin Coatings, *Ceram. Int.*, 2000, **26**(7), p 787–795. [https://doi.org/10.1016/S0272-8842\(00\)00015-8](https://doi.org/10.1016/S0272-8842(00)00015-8)
22. W. Aperador, Estudio de la Resistencia a la Corrosión Electroquímica de Electro-recubrimientos Niquel/Cobre Obtenidos por Corriente Pulsante, *Ing. y Desarrollo*, 2010, **27**, p 48–61.
23. A. Vargas, W. Aperador, C. Ortiz, J. Betancur and C. Wang, Caracterización Electroquímica de Fernal Expuesto a Condiciones Corrosivas–Erosivas, *Rev. Latinoam. Metalurg. Mater.*, 2009, **1**(S1), p 149–155.
24. P.E. Hovsepian et al., TiAlN/VN Superlattice Structured PVD Coatings: A New Alternative in Machining of Aluminium Alloys for Aerospace and Automotive Components, *Surf. Coat. Technol.*, 2006, **201**(1–2), p 265–272. <https://doi.org/10.1016/J.SURFCOAT.2005.11.106>
25. W. Aperador, J.C. Caicedo, C. España, G. Cabrera and C. Amaya, Bilayer Period Effect on Corrosion–Erosion Resistance for $[\text{TiN}/\text{AlTiN}]_n$ Multilayered Growth on AISI 1045 Steel, *J. Phys. Chem. Solids*, 2010, **71**(12), p 1754–1759. <https://doi.org/10.1016/J.JPCS.2010.08.019>
26. V. Bonu, M. Jeevitha, V. Praveen Kumar and G. Srinivas, Solid Particle Erosion and Corrosion Resistance Performance of Nanolayered Multilayered Ti/TiN and TiAl/TiAlN Coatings Deposited on Ti6Al4V Substrates, *Surf. Coat. Technol.*, 2020, **387**, p 125531. <https://doi.org/10.1016/j.surfcoat.2020.125531>
27. J.C. Caicedo, G. Cabrera, H.H. Caicedo, C. Amaya and W. Aperador, Nature in Corrosion–Erosion Surface for $[\text{TiN}/\text{TiAlN}]_n$ Nanometric Multilayers Growth on AISI 1045 Steel, *Thin Solid Films*, 2012, **520**(13), p 4350–4361. <https://doi.org/10.1016/j.tsf.2012.02.061>
28. W.A. Chaparro, C.R. Martin and E.V. López, Synergy Between Erosion–Corrosion of Steel AISI 4140 Covered by a Multilayer TiCN / TiNbCN, at an Impact Angle of 90° , *Dyn.*, 2013, **80**(178), p 101–108.

Publisher's Note Springer Nature remains neutral with regard to jurisdictional claims in published maps and institutional affiliations.